# Steel alloy hot roll simulations and through thickness variation using dislocation density based modeling.

G.J. JANSEN VAN RENSBURG, S. KOK and D.N. WILKE

**Abstract**

Different roll pass reduction schedules have different effects on the through thickness properties of hot rolled metal slabs. In order to assess or improve a reduction schedule using the finite element method, a material model is required that captures the relevant deformation mechanisms and physics. The model should also report relevant field quantities to asses variations in material state throughout the thickness of a simulated rolled metal slab. In this paper, a dislocation density based material model with recrystallization is presented and calibrated on the material response of a high strength low alloy steel. The model has the ability to replicate and predict material response to a fair degree thanks to the physically motivated mechanisms it is built on. An example study is also presented to illustrate the possible effect different reduction schedules could have on the through thickness material state and the ability to asses these effects based on finite element simulations.

## 1 Introduction

Functional grading or homogeneity of the through thickness material micro-structure is an important factor that determines the mechanical properties of hot rolled metal products [1]. The thickness of a metal slab can be reduced by any number of subsequent roll passes and interpass times at a specific temperature to reach a final desired slab thickness and through thickness micro-structure. To asses the effect of a specific reduction schedule on the through thickness micro-structure of a hot rolled plate, a finite element analysis (FEA) can be performed [2, 3]. A material model that captures all of the relevant deformation mechanisms and physics is required to do this successfully. There are various options available to model recrystallization during the finite element simulation of a hot rolling or roughing processes. These options vary in terms of computational complexity, resolution and fidelity with which the effect of different reduction schedules could be investigated.

One option could be to link multiple model resolutions. Multi scale recrystallization modeling strategies could involve linking a finite element code with Monte Carlo Potts [4, 5], cellular automaton [6, 7, 8], phase field models [9, 10, 11, 12], vertex or front-tracking [13, 14] as well as level set methods [15, 16]. Linking polycrystal-plasticity with recrystallization to a hot roll reduction simulation may give detailed results on the effect of different roll reduction schedules on the resulting through thickness stock variation. The computational complexity and expense of a detailed multi-resolution approach is however an aspect that should be taken into account. As an alternative, a unified set of continuum equations or mean field approach to micro-structure evolution and material response may be considered.

Baron *et al.* [17] develop and use a continuum model to represent the micro-structure evolution with dynamic recrystallization of a high strength martensitic steel. The strong dependence of the dynamic recrystallization kinetics on the initial micro-structure were taken into account during their model development. Another continuum material model by Lin *et al.* [2] makes use of a normalized dislocation density variable coupled with evolution equations on the average grain size as well as recrystallized volume fraction. Lin *et al.* [2] used a set of unified viscoplastic equations to model a two roll-pass reduction schedule. This continuum model was also recently used to model the micro-structural evolution during hot cross wedge rolling [18] illustrating the continued usefulness and relevance of continuum based recrystallization models in the finite element simulation of material processing.

G.J. JANSEN VAN RENSBURG, PhD Researcher, is with CSIR Modelling and Digital Science, Meiring Naudé Road, 0184 Pretoria, South Africa, Contact e-mail:jjvrensburg@csir.co.za S. KOK and D.N. WILKE, Professor and Senior Lecturer, are with at the Department of Mechanical and Aeronautical Engineering, University of Pretoria, Lynnwood Road, 0083 Pretoria, South Africa

Mean field recrystallization models may also be implemented into a finite element environment and assessed at each material integration point. Using the models of Montheillet *et al.* [19] or Bernard *et al.* [20] for example, discontinuous dynamic recrystallization may be approached by modeling macroscopic material response as an averaged result over a representative set of spherical grains. In their models, they consider different evolution equations for the dislocation density, stress - strain relationship and grain size evolution. Each grain has a set of state variables to represent grain size and dislocation density. A grain either grows or shrinks as a result of interaction with the surrounding material, typically idealized using mean field values. During recrystallization, new grains are nucleated using a phenomenological rate equation. Riedel and Svoboda [21] on the other hand use a Chaboche-type hardening law per grain instead of dislocation density. New grains can nucleate within existing material once sufficiently high energy density allows it. Grain growth as a result of grain boundary energy and pinning as a result of the precipitation and dissolution of particles are also taken into account.

In this paper, the material response of a high strength low alloy (HSLA) micro-alloyed steel is modeled using a dislocation density based model with recrystallization [22]. The model has the ability to represent multiple waves of recrystallization at a single integration point. A unique set of internal state variables (ISVs) are associated with the original and each volume fraction of recrystallized material per integration point. The equivalent continuum response is then determined using the volume fraction averaged ISVs, similar to the model validated by Brown and Bammann [23].

The data and material are discussed in the second section of this paper. The experimental test data was obtained on cylindrical test specimens in compression. The material is a C-Mn-Nb-Ti-V micro-alloyed steel. Extensive data is available on the hardening, recovery and static recrystallization of the alloy in the austenite ($\gamma$-Fe) phase for different compression schedules [24]. The test data has various amounts of straining with various waiting times between each additional compression. In the times between reduction the material undergoes static recrystallization.

The dislocation density based material model with recrystallization is discussed in Section 3 while the model parameters are identified that best represent the static recrystallization observed in the experimental material response in Section 4. The parameters are identified using numerical optimization and candidate material response modeled using a material point based simulation.

Section 5.1 is devoted to the FEA of a specific experimental test schedule. An axisymmetric experimental setup is first modeled so the global response and material point simulation can be compared to the experimental response. This is followed by a roll pass reduction simulation as well as a comparison on the through thickness internal state variation as a result of different slab reduction schedules.

# 2 Data

The influence of the strain sequence during hot slab rolling or roughing was investigated by Maubane *et al.* [24] using different experimental compression sequences on cylindrical test specimens. These experimental test responses were made available for the work done in this paper. The alloy chemistry considered is made up of 0.134% C, 1.5% Mn, 0.38% Si, 0.04% Nb, 0.025% Ti, 0.028% V, 0.049% Al, 55ppm N and 41ppm S. The reheating and roughing experiments were conducted in a Bähr deformation dilatometer. Maubane *et al.* [24] used a constant austenizing temperature, constant soaking time, various heating rates and different compression sequences to mimic the roughing strain sequences they were interested in.

Each of the reductions were performed at a slightly higher strain rate compared to the one before. The cylindrical specimens tested were approximately 10mm high with a diameter of 5mm. Maubane *et al.* [24] experimented on six different reduction schedules. The first schedule, here labeled schedule $I$, consists of 14 reductions of 7% each. The reduction rates start at $0.3\text{s}^{-1}$ for the first 7% and then increases with $0.2\text{s}^{-1}$ each next reduction to end at a rate of $2.9\text{s}^{-1}$ for the fourteenth compression. During the sequence, the temperature slowly decreases to represent a cool down of the metal slab. Schedule $II$ consists of 10 reductions of 10% each while schedule $III$ consists of 6×15% reductions. Additional schedules tested experimentally repeated the 7%, 10% and 15% reduction sequences op to a point followed by one large final reduction of 40%, i.e. schedule $IV$: 8×7%+40%, schedule$V$: 6×10%+40% and schedule $VI$: 4×15%+40%.

Some of the schedules were performed multiple times with different waiting or interpass times between additional straining. Three different data sets are available for schedule $VI$ for example. After a starting temperature of 1423K(1150°C) is reached, the tests were done with different interpass times. In the one case the interpass time between each subsequent compression was approximately 9 to 10 seconds. Another test had a waiting period of approximately 20 seconds between each compression while another

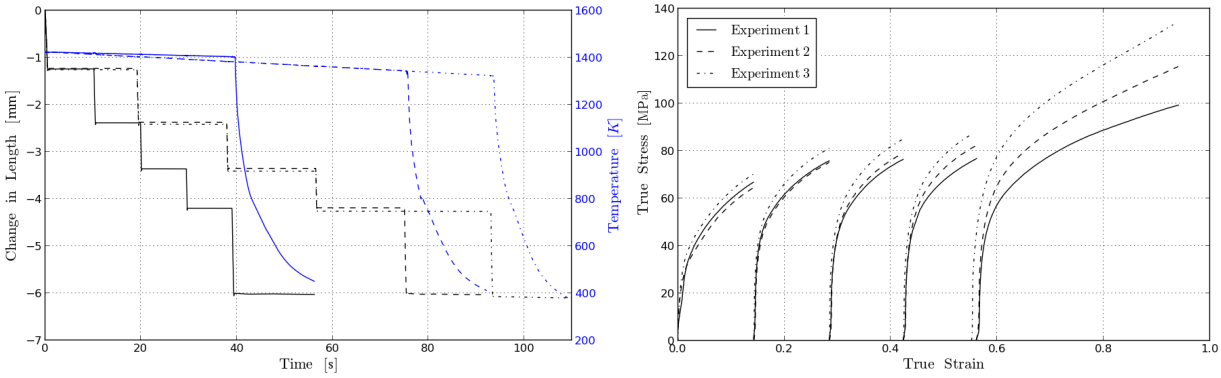


(a) (b)

Figure 1: Different results for three schedule $VI$ experiments with varying interpass time. (a) The change in length and temperature once 1423K(1150°C) was reached and (b) corresponding true stress - true strain curves.

waited 40 seconds between the fourth and fifth compression step. The change in length and change in temperature from the initial compression for the three different experiments for schedule $VI$ are visible in Figure 1(a). A constant decrease in temperature of about $0.5\text{Ks}^{-1}$ is visible throughout the experiment before the specimen is quenched.

The true stress - true strain data for the same three compression tests is displayed in Figure 1(b). This figure indicates to some degree the temperature dependence of the material response. It also indicates the potential variability in the material response as seen in the first compression steps, all measured for the same strain rate and temperature. At the end of the first compression step, the true stress values in Figure 1(b) for the three different experiments are 67.26MPa, 64.84MPa and 70.54MPa with an average value of 67.55MPa. This translates to a possible variation in material response of $(70.54 - 64.84)/67.55 \approx 8.44\%$ despite subjecting the same material to the same temperature and strain history. The potential variability continues in the first four compression steps of the experiments with 20 second wait between compression. These experimental results are visible as the dashed and dash-dot lines in Figures 1(a) and (b) respectively. The first four reductions resulted in different responses in Figure 1(b) despite being subjected to similar temperatures and strains according to Figure 1(a). The different material response data available is used to calibrate a dislocation density based material model for later use in roll schedule simulations. This strain rate and temperature dependent state variable based material model is covered in the following section before characterizing the model on the experimental material response data.

# 3 Dislocation based model

The material model is coded into an elastic trial - radial return type algorithmic implementation user material (`UMAT`) for $J_2$ isotropic hypo-elastoplasticity [22]. In general, the components of the total strain rate tensor $\dot{\varepsilon}_{ij}$ within the model framework are additively decomposed into elastic $\dot{\varepsilon}^{\mathrm{e}}_{ij}$ and plastic $\dot{\varepsilon}^{\mathrm{p}}_{ij}$ components

$$\dot{\varepsilon}_{ij} = \dot{\varepsilon}^{\mathrm{e}}_{ij} + \dot{\varepsilon}^{\mathrm{p}}_{ij}. \tag{1}$$

The elastic part obeys Hooke's law

$$\dot{\varepsilon}^{\mathrm{e}}_{ij} = C^{-1}_{ijkl}\dot{\sigma}_{kl}, \qquad \text{where} \qquad C^{-1}_{ijkl} = \frac{1}{2\mu}\left(\delta_{ik}\delta_{jl} - \frac{\nu}{1+\nu}\delta_{ij}\delta_{kl}\right) \tag{2}$$

with $\dot{\sigma}_{ij}$ the time derivative of the stress tensor, $\mu$ is the shear modulus, $\nu$ is Poisson's ratio and $\delta_{ij}$ represents Kronecker's delta. The temperature dependent shear modulus is determined using the model developed by Varshni [25]

$$\mu(T) = \mu_r - \frac{D_r}{\exp\left(T_r/T\right) - 1}, \tag{3}$$

where $\mu_r$, $D_r$ and $T_r$ are reference material constants while $T$ is the absolute temperature. The plastic part of the strain rate tensor takes the form of the Lévy-von Mises equation

$$\dot{\varepsilon}_{ij}^{\mathrm{p}} = \frac{3}{2}\frac{\dot{\alpha}}{\sigma_{\mathrm{vM}}} s_{ij}, \tag{4}$$

where $s_{ij}$ are the components of the deviatoric stress, $\dot{\alpha}$ is the scalar equivalent plastic strain rate and $\sigma_{\mathrm{vM}}$ the von Mises equivalent stress. The temperature and rate dependent effective yield stress is determined using

$$\sigma_{\mathrm{y}} = \hat{\sigma}_a + S_\varepsilon(\dot{\alpha}, T)\hat{\sigma}_\varepsilon \tag{5}$$

where $\hat{\sigma}_\varepsilon$ represents the evolving thermal component of the threshold stress representing the material state. $\hat{\sigma}_a$ represents an athermal stress component while $S_\varepsilon$ is a temperature and equivalent strain rate dependent scaling function [26]

$$S_\varepsilon(\dot{\alpha}, T) = \frac{\mu}{\mu_r}\left[1 - \left[\frac{T}{a_0 \mu}\ln\left(\frac{\dot{\varepsilon}_0}{\dot{\alpha}}\right)\right]^{1/q}\right]^{1/p}. \tag{6}$$

In Equation (6), $a_0$ is a grouped constant introduced here to replace $g_0 b^3/k_{\mathrm{B}}$ in the formulation by Follansbee and Kocks [26] where $g_0$ is the normalized activation energy, $b$ is the length of the Burgers' vector and $k_{\mathrm{B}}$ is the Boltzmann constant. $\dot{\varepsilon}_0$ is taken as a material constant associated with the mobility of dislocations while $p$ and $q$ are statistical parameters that characterize the shape of the obstacle profile [26]. Evolution of a thermal stress component $\hat{\sigma}_\varepsilon$ in Equation (5) completes the constitutive formulation.

An ISV choice is made by following the work done by Estrin [27]. In this modeling approach a stress like constant $\sigma_0$ is introduced associated with a reference dislocation density $\rho_0$. This construct allows formulation of the constitutive model using the dislocation density ratio ISV $\varrho = \rho/\rho_0$ and dislocation density based evolution equations. The evolving thermal component of the threshold stress $\hat{\sigma}_\varepsilon$ in Equation (5) is related to the dislocation density ratio ISV by

$$\hat{\sigma}_\varepsilon = \sigma_0\sqrt{\varrho}. \tag{7}$$

In this paper, a dislocation density based model with recrystallization [22] is used. The material model is based on a two ISV model similar to the one used by Kok *et al.* [28] with dislocation density ratio $\varrho$ and average slip plane lattice incompatibility $\lambda$ chosen as the two ISVs. The model is further expanded by including terms for thermal recovery and multiple cycles of recrystallization.

### 3.1 Two state variable model

In this subsection the two ISV based model is first considered without the effects of recrystallization. The mean distance a mobile dislocation travels before it is immobilized at impenetrable obstacles is called the mean free path [29]. While the statistically determined mean free path $L_s$ relates to the total dislocation density $\rho$ through $L_s \propto 1/\sqrt{\rho}$, a geometrically determined mean free path $L_g$ relates to the average slip plane lattice incompatibility $\lambda$ through

$$L_g \propto \left(\frac{1}{\lambda}\right)^{r_g} \tag{8}$$

where $1/2 \leq r_g \leq 1$ is a parameter [28]. The evolution of the average slip plane lattice incompatibility following Kok *et al.* [28] is further

$$\dot{\lambda} = \dot{\alpha} C_\lambda, \tag{9}$$

where $C_\lambda$ is a constant associated with a specific grain size. Combining the modified evolution equation for statistically stored dislocation density $\rho$ as used by Kok *et al.* [28] with a static thermal recovery term similar to that used by Song and McDowell [30], the rate form of an evolution equation for the dislocation density ratio $\varrho = \rho/\rho_0$ in Equation (7) is [22]

$$\dot{\varrho} = \dot{\alpha}\left(C_0\lambda^{r_g} + C_1\sqrt{\varrho} - C_2(\dot{\alpha}, T)\varrho\right) - C_3(T)\varrho^{r_3}. \tag{10}$$

In this rate equation $C_0$ and $C_1$ are constants associated with the geometrically and statistically derived dislocation storage terms. $C_2(\dot{\alpha}, T)$ is a rate and temperature dependent dynamic recovery function

while $C_3(T)$ is a static recovery term with dislocation effect captured by the exponent $r_3$. Using the dynamic recovery function of the Mechanical Threshold Stress model [26], an analog in the current model formulation is achieved using

$$C_2(\dot{\alpha}, T) = C_{20} \exp\left[-\frac{T}{a_{02}\mu} \ln\left(\frac{\dot{\alpha}}{\dot{\varepsilon}_{02}}\right)\right]. \tag{11}$$

In Equation 11, $C_{20}$, $\dot{\varepsilon}_{02}$ and $a_{02}$ are material constants. Static thermal recovery is modeled by an Arrhenius expression similar to the one used by Song and McDowell [30]

$$C_3(T) = C_{30} \exp\left(-\frac{a_{03}}{T}\right), \tag{12}$$

where $C_{30}$ and $a_{03}$ are constants.

## 3.2 Modeling Recrystallization

A material has an initial volume fraction $f_{\mathrm{x}_0} = 1$ that has recrystallized 0 times. The material can then also have a once recrystallized volume fraction $f_{\mathrm{x}_1}$ that replaces a certain amount of the original material. This amount of material replaced can not be more than the original material meaning $0 \leq f_{\mathrm{x}_1} \leq f_{\mathrm{x}_0}$. For multiple waves of recrystallization, this means that a total volume fraction of material recrystallized $i+1$ times would be smaller than the total volume fraction recrystallized $i$ times, i.e. $0 \leq f_{\mathrm{x}_{i+1}} \leq f_{\mathrm{x}_i}$ in general.

Each material volume fraction $f_{\mathrm{x}_i}$ has it's own set of two ISVs $\varrho_{\mathrm{x}_i}$ and $\lambda_{\mathrm{x}_i}$. These ISVs affect the growth rate of the next wave of recrystallization $\dot{f}_{\mathrm{x}_{i+1}}$. The growth rate of a volume fraction recrystallized $i+1$ times is modeled from the work by Cahn and Hagel [31] using

$$\dot{f}_{\mathrm{x}_{\mathrm{i}+1}} = A_{\mathrm{x}_{\mathrm{i}+1}} v_{\mathrm{x}_{\mathrm{i}+1}}, \tag{13}$$

where $A_{\mathrm{x}_{\mathrm{i}+1}}$ is the interfacial area between regions recrystallized $i+1$ and $i$ times [23]. This is multiplied by the average boundary velocity of the interface sweeping through the region $v_{\mathrm{x}_{\mathrm{i}+1}}$. The average grain boundary velocity is in turn expressed using the driving pressure $P$ for boundaries with a specific energy and mobility $M$ [32]. Using the empirical form of Chen *et al.* [33] the grain boundary mobility associated with $v_{\mathrm{x}_{i+1}}$ is [22]

$$M_{\mathrm{x}_{i+1}} = M_0 \exp\left(-\frac{a_{0\mathrm{Rx}}}{T}\right)\left[1 - \exp\left(-C_{\mathrm{Rx}\lambda 0}\lambda_{\mathrm{x}_i}^{r_{\mathrm{Rx}\lambda}}\right)\right], \tag{14}$$

where $M_0$, $a_{0\mathrm{Rx}}$, $C_{\mathrm{Rx}\lambda 0}$ and the exponent $r_{\mathrm{Rx}\lambda}$ are constants.

The driving force behind the interfacial grain boundary velocity is the stored energy in the dislocation structure. According to Humphreys and Hatherley [34], the pressure driving the subgrain boundary growth can in it's simplest form be expressed as $P = \mu b^2 \rho/2$. This assumes that the boundary energy effects on the driving force are negligible. Considering the dislocation density ratio used as evolving ISV in the current framework, the driving pressure pressure associated with $v_{\mathrm{x}_{i+1}}$ is calculated by

$$P_{\mathrm{x}_{i+1}} = \frac{1}{2}\mu b^2 \rho_0 \varrho_{\mathrm{x}_i}. \tag{15}$$

Following the work done by Brown and Bammann [23], the grain boundary interfacial area between the volume fractions recrystallized $i$ and $i+1$ times is determined using the function

$$g(f_{\mathrm{x}_i}, f_{\mathrm{x}_{i+1}}) = f_{\mathrm{x}_i}\left(\frac{f_{\mathrm{x}_{i+1}}}{f_{\mathrm{x}_i}}\right)^{r_{\mathrm{Rx}a}}\left(1 - \frac{f_{\mathrm{x}_{i+1}}}{f_{\mathrm{x}_i}}\right)^{r_{\mathrm{Rx}b}}\left(1 + C_{\mathrm{Rx}c}\left(1 - f_{\mathrm{x}_i}\right)\right) \tag{16}$$

with $A_{\mathrm{x}_{i+1}} \propto g(f_{\mathrm{x}_i}, f_{\mathrm{x}_{i+1}})$. $r_{\mathrm{Rx}a}$ and $r_{\mathrm{Rx}b}$ are exponents used in the empirical relation of the interfacial grain boundary area while $C_{\mathrm{Rx}c}$ is a constant. Including all of the above mentioned into a single expression, the rate of recrystallization in Equation (13) is rewritten for the volume fraction recrystallized $i+1$ times

$$\dot{f}_{\mathrm{x}_{i+1}} = \varrho_{\mathrm{x}_i} C_{\mathrm{Rx}0} C_{\mathrm{Rx}T}(T) C_{\mathrm{Rx}\lambda}\left(\lambda_{\mathrm{x}_i}\right) g(f_{\mathrm{x}_i}, f_{\mathrm{x}_{i+1}}). \tag{17}$$

The function is rewritten so that $C_{\mathrm{Rx}0}$ effectively contains all the pre-exponential constants. Similarly $C_{\mathrm{Rx}T}(T)$ contains the temperature dependence in a single function

$$C_{\mathrm{Rx}T}(T) = \mu\left(T\right) \exp\left(-\frac{a_{0\mathrm{Rx}}}{T}\right). \tag{18}$$

The function $C_{\mathrm{Rx}\lambda}(\lambda)$ contains the geometric effects in the rewritten function

$$C_{\mathrm{Rx}\lambda}(\lambda) = 1 - \exp\left(-C_{\mathrm{Rx}\lambda 0}\lambda^{r_{\mathrm{Rx}\lambda}}\right). \tag{19}$$

In the event of recrystallization, the ISV evolution equations are different to Equations (9) and (10). Given a time increment $\delta t$, the first $f_{\mathrm{x}_1}$ and second $f_{\mathrm{x}_2}$ volume fractions can both progress for example, meaning region $f_{\mathrm{x}_1} - f_{\mathrm{x}_2}$ will increase by $\delta f_{\mathrm{x}_1}$ and decrease by $\delta f_{\mathrm{x}_2}$. Assuming recrystallization removes the dislocation structure, the dislocation density ratio within a newly recrystallized portion $\delta f_{\mathrm{x}_1}$ should be reinitialized. Applying the rule of mixtures as done by Brown and Bammann [23], the rate form of the dislocation density ratio evolution equation in Equation (10) is replaced by

$$\dot{\varrho}_{\mathrm{x}_i} = \dot{\alpha}\left(C_0\lambda_{\mathrm{x}_i}^{r_g} + C_1\sqrt{\varrho_{\mathrm{x}_i}} - C_2(\dot{\alpha},T)\,\varrho_{\mathrm{x}_i}\right) - C_3(T)\varrho_{\mathrm{x}_i}^{r_3} - \frac{\dot{f}_{\mathrm{x}_i}}{f_{\mathrm{x}_i} - f_{\mathrm{x}_{i+1}}}\varrho_{\mathrm{x}_i} \tag{20}$$

for the dislocation density ratio variable associated with the volume fraction $f_{\mathrm{x}_i}$. Similarly for the average slip plane lattice incompatibility ISV

$$\dot{\lambda}_{\mathrm{x}_i} = \dot{\alpha}C_\lambda - \frac{\dot{f}_{\mathrm{x}_i}}{f_{\mathrm{x}_i} - f_{\mathrm{x}_{i+1}}}\lambda_{\mathrm{x}_i}. \tag{21}$$

If multiple volume fractions are active the equivalent threshold stress in Equation (7) is calculated from the average dislocation density ratio

$$\bar{\varrho} = \sum_{i=0}^{n_{\mathrm{x}}-1} \varrho_{\mathrm{x}_i}\left(f_{\mathrm{x}_i} - f_{\mathrm{x}_{i+1}}\right), \tag{22}$$

where $n_{\mathrm{x}}$ is the total number of recrystallization cycles. The same can be done for the equivalent plastic strains and average slip plane lattice misorientation ISVs so that volume fraction averaged values are

$$\bar{\alpha} = \sum_{i=0}^{n_{\mathrm{x}}-1} \alpha_{\mathrm{x}_i}\left(f_{\mathrm{x}_i} - f_{\mathrm{x}_{i+1}}\right) \quad \text{and} \quad \bar{\lambda} = \sum_{i=0}^{n_{\mathrm{x}}-1} \lambda_{\mathrm{x}_i}\left(f_{\mathrm{x}_i} - f_{\mathrm{x}_{i+1}}\right). \tag{23}$$

In this model, the dislocation density and lattice misorientation ISVs are used in the material response calculation while the accumulated plastic strain is simply an accumulation of all of the plastic strain increments experienced from the moment a specific volume fraction is activated.

The model is implemented into an Abaqus `UMAT` subroutine as well as a one dimensional version used for the material parameter characterization in the following section.

# 4 Fitting the data

In general, the experimental stress - strain data is fit above a strain value of 0.01 or additional 0.01 strain for each subsequent compression curve. For a given set of material parameter values, here just referred to as the vector $\mathbf{x}$, the model is evaluated for the same temperatures and strain rates as the experimental data. The stress values at each of the $N$ valid data points are then compared to the predicted stress value to construct an objective function.

The objective function is assembled by comparing the model predicted stress value $\sigma_i^{\mathrm{model}}$ to the associated stress value of the $i^{th}$ valid data point $\sigma_i^{\mathrm{data}}$. The objective function used for the parameter identification is

$$f_{\mathrm{obj}}(\mathbf{x}) = \sum_{i=1}^{N}\left(\frac{\sigma_i^{\mathrm{model}}(\mathbf{x}) - \sigma_i^{\mathrm{data}}}{\sigma_i^{\mathrm{data}}}\right)^2. \tag{24}$$

Initial material parameter values are chosen and then improved by minimizing this objective function. Material parameter value constraints are also assigned. The parameter identification is performed using the the downhill simplex method. If a constraint is violated, the objective function is penalized.

Not all of the data is used in the characterization. A single data set for each roughing schedule is modeled and compared. The model outputs and experimental data for all the different data sets on schedules $I$ to $VI$ are illustrated in Figure 2. In Figure 2, the green curves represent the material model response used to evaluate the objective function on a subset of the data. The red curves in Figure 2 are predicted responses using the material model. In this figure the benefit of this physically developed state variable based model is visible in its ability to not only model but also predict material response.

The material parameter values resulting in the fit given in Figure 2 are :

- The elastic properties using the shear model relationship in Equation (3) are $\mu_r = 85908$GPa, $D_r = 6758.8$GPa, $T_r = 180$K and a Poisson's ratio of $\nu = 0.29$.
- The temperature and rate dependent scaling function in Equation (6) is modeled with $a_{0\varepsilon} = 1.4343$K/MPa, $p_\varepsilon = 0.5914$, $q_\varepsilon = 1.0973$ , and $\dot{\varepsilon}_{0\varepsilon} = 10^7 \text{s}^{-1}$.
- The athermal yield stress component and reference stress values using Equation (5) are $\hat{\sigma}_a = 11.175$MPa and $\sigma_0 = 82.126$MPa.
- The evolution of $\bar{\lambda}$ according to Equation (21) is again modeled using $C_{\lambda \text{x}} = 1$.
- The parameters associated with the evolution of the dislocation density ratio in Equation (20) are $C_g = 4369.3$, $r_g = 0.5701$, $C_1 = 146.63$, $C_{20} = 41.47$, $a_{02} = 0.5413$K/MPa, $\dot{\varepsilon}_{02} = 10^3 \text{s}^{-1}$, $C_{30} = 1.6078 \times 10^9 \text{s}^{-1}$, $a_{03} = 36257$K and $r_3 = 2$.
- The recrystallization parameters are $C_{\text{Rx}0} = 4352.8 \text{s}^{-1}$ for the constant in Equation (17), $a_{0\text{Rx}} = 33092$K in (18) with $C_{\text{Rx}\lambda 0} = 549.21$ and $r_{\text{Rx}\lambda} = 2.519$ in Equation (19). The equivalent interfacial subgrain boundary area function in Equation (16) is modeled using $r_{\text{Rx}a} = 0.2874$, $r_{\text{Rx}b} = 1.0001$ and $C_{\text{Rx}c} = 17.935$.

The material parameter values used to model the different schedules do a satisfactory job of reproducing the data given the expected material variability of about 8.44% observed in Section 2. In some cases an accurate representation of the strain hardening, static recrystallization and thermal dependence is captured by the model.

The internal state variable evolution using the calibrated material model for the schedule $VI$ strain roughing sequence with approximately 10 second interpass time is given again in Figure 3. The recrystallized volume fractions for the multiple waves of recycling are given in (a) over the time history and in (b) over the strain history.

The first wave of static recrystallization results in an approximately 58% recrystallized material after the first 9.625 second wait. After the second reduction and subsequent 9.4023 second wait, the material model indicates that the original material is replaced by more that 90% recrystallized material. Approximately 70% of the material has also undergone a second wave of recrystallization. After about 39 seconds into the experiment, the model indicates that the original material has been virtually replaced with a new micro-structure where more than 80% of the material has seen four waves of recrystallization.

Figures 3(c) and (d) indicate the dislocation density ratio state variables per recrystallized volume fraction over the time and strain history respectively. Apart from the static recrystallization, there is also a significant amount of thermal recovery in the predicted material response. In Figure 3(c) the dislocation density self diffusion over time is visible while Figure 3(d) indicates the dislocation density evolution per volume fraction. In Figures 3(e) and (f) the average slip plane lattice misorientation over the time and strain histories are presented. This internal state variable evolves as in Equation (21) with $C_{\lambda \text{x}} = 1$. This means that in the absence of recrystallization $\dot{\bar{\lambda}} = \dot{\alpha}$, as seen in the straight line in Figure 3(f) for $\bar{\lambda}_{\text{x}_0}$. The reduction in this ISV as a function of time is an indication of the effect of the static recrystallization on the average slip plane lattice misorientation of the recrystallized material using the rule of mixtures.

Up to this point all of the results are material point simulator based. Next, the schedule $VI$ strain roughing sequence with approximately 10 second interpass time is modeled in detail using Abaqus. This is done using the experimental die displacement and response histories to create different steps and boundary conditions. The material parameter values in this section are used with the Abaqus `UMAT` based on the model in the previous section.

# 5 Finite Element Modeling

## 5.1 Axisymmetric compression

Using the material model parameters determined in Section 4, an FEA of the experimental test is performed to inspect the difference in response when a detailed simulation is considered instead of a single point integration.

The experimental compression tests were done on cylindrical specimens 10mm high with a diameter of 5mm as illustrated in Figure 4(a). The finite element analysis is therefore done using an axisymmetric

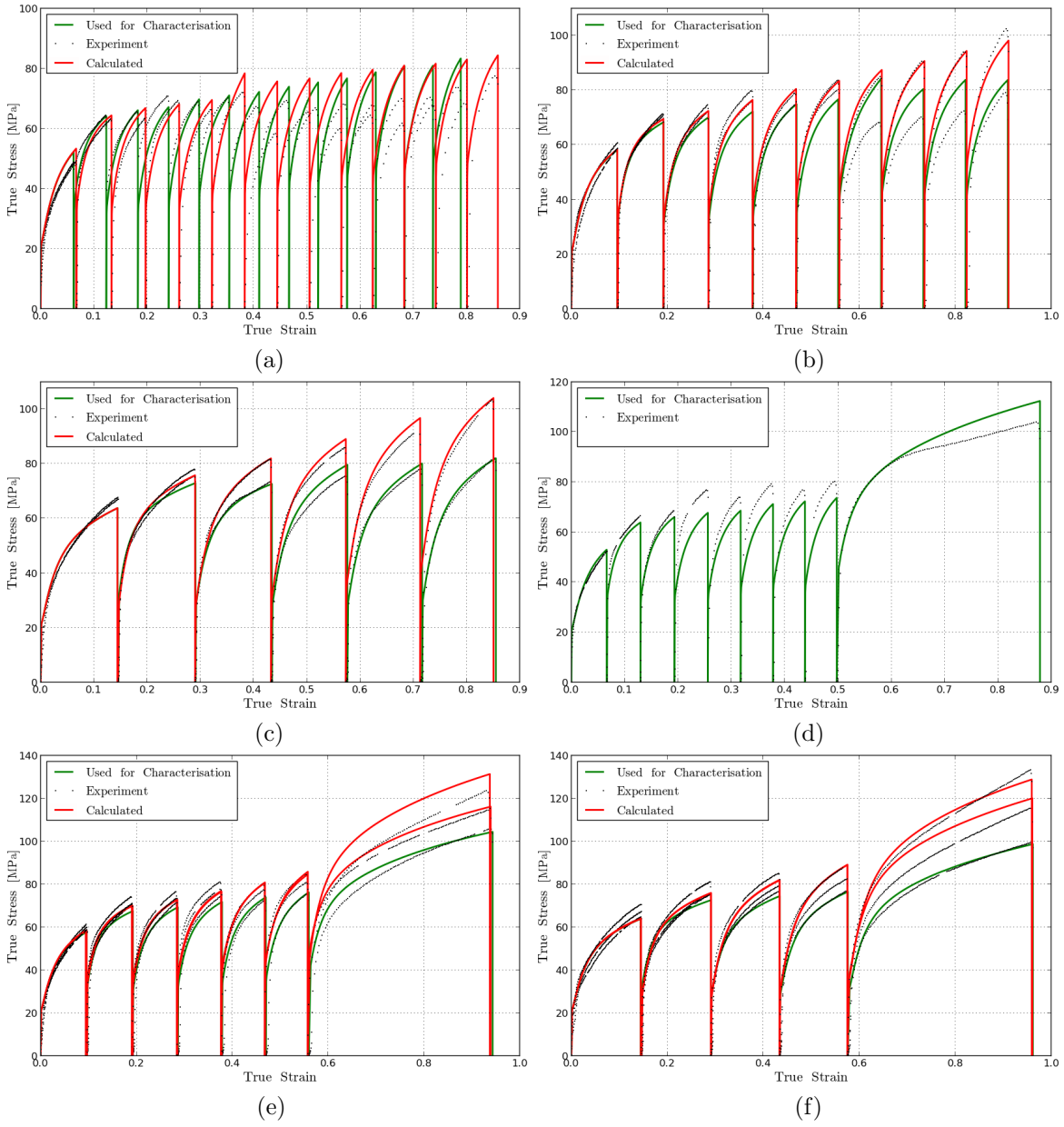


Figure 2: Model response compared to the experimental data for schedule (a) $I$ (b) $II$ (c) $III$ (d) $IV$ (e) $V$ (f) $VI$

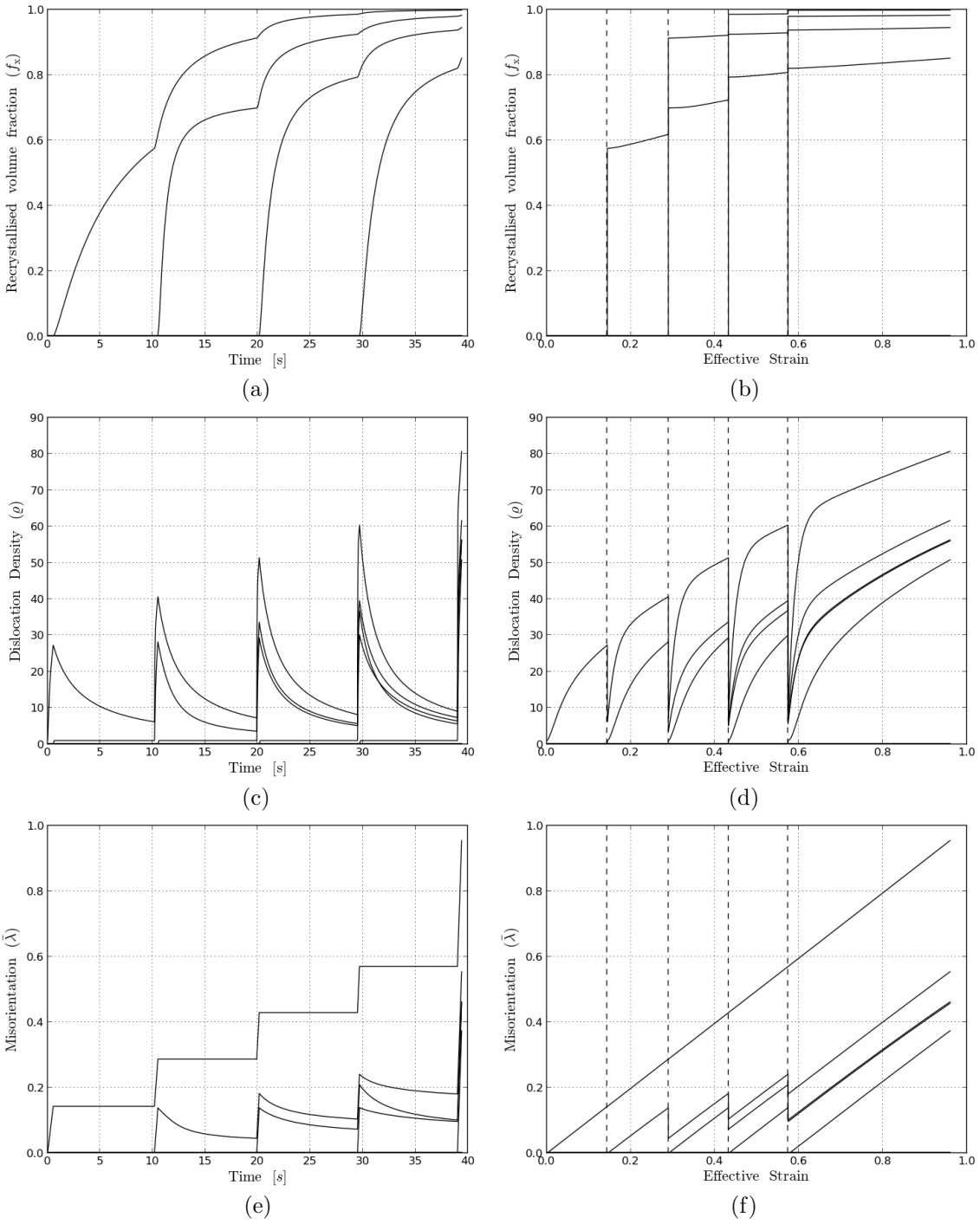


Figure 3: Internal state variable evolution for the the schedule $VI$ data with an approximate 10 second wait time between each reduction. (a,b) Recrystallized volume fraction; (c,d) dislocation density ratio and (e,f) average slip plane lattice misorientation over time and strain histories.

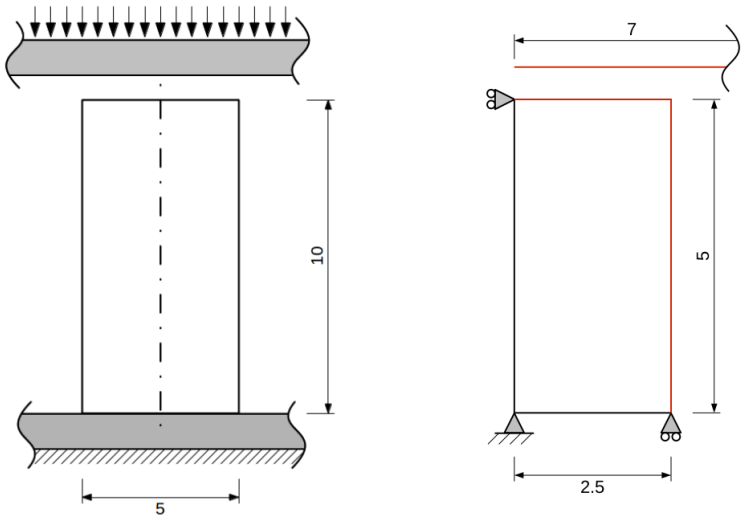


(a) (b)

Figure 4: (a) Compression of a cylindrical test specimen and (b) axisymmetric boundary value problem equivalent.

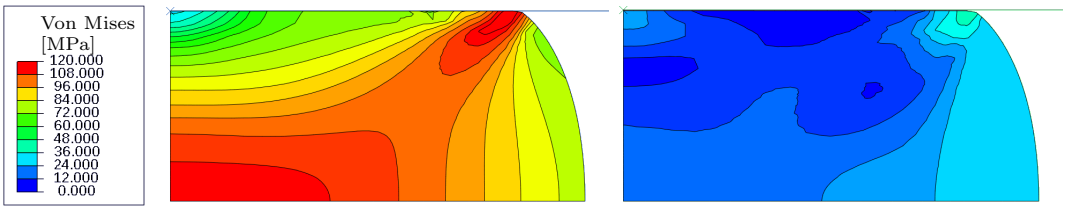


(a) (b)

Figure 5: Von Mises stress contours on the compressed axisymmetric billet at (a) 39.3994s and (b) 10 seconds afterwards.

boundary value problem equivalent with contact illustrated in Figure 4(b). A quarter axisymmetric model 5mm high with a 2.5mm radius is modeled. From the temperature history in Figure 1, a linear change in temperature is modeled starting at 1423K and ending with 1400K at a total time of 40 seconds.

The experimental data values are used to set up different modeling steps and boundary conditions. Five compression steps and five wait steps are set up. The contact surface is initially in contact with the top surface of the axisymmetric test specimen model and a friction coefficient $\mu_{\text{frict}} = 0.3$ is assumed.

The die is modeled using a 7mm long rigid analytical surface while the axisymmetric billet is modeled using 925 linear axisymmetric stress elements with full integration. The elements have an initial width to height ratio of approximately 1:1.5 meaning the specimen is discretized using 25 elements through the radius and 37 through its height.

In a compression step the displacement of the rigid contact surface is prescribed to represent the total strain applied. In a waiting step, the surface is first displaced 0.01mm in a 0.01s interval so that it is no longer in contact with the material. After waiting the required amount of time, the next compression step is modeled. The step times, total simulation time, equivalent and prescribed die displacement is given in Table **??**.

In Figure 5, the equivalent von Mises stress distribution is displayed at the end of the compression (39.3994s) as well as 10 seconds afterwards. The same is done for the equivalent plastic strain contours in Figures 6.

The stresses are displayed between 0MPa and 120MPa in Figure 5(a) and (b). The equivalent plastic strain contours in Figures 6(a) and (b) are displayed for the same range between 0 and 0.7. Comparing Figure 6(a) to Figure 6(b) the amount of strain recovered if an additional 10 seconds are allowed for recrystallization is illustrated while the dislocation structure is reset due to both thermal recovery and recrystallization. In Figure 7, the internal state variables associated with the active recrystallized volume

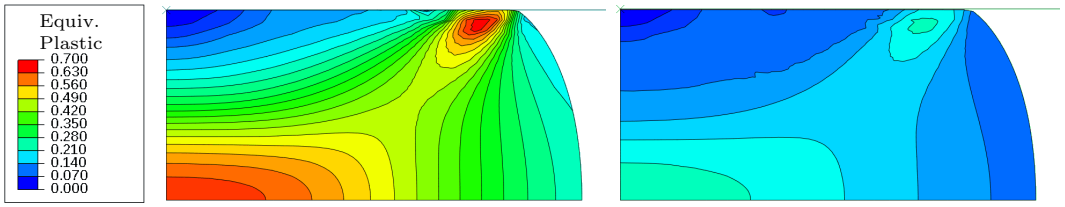


Figure 6: Equivalent plastic strain contours on the compressed axisymmetric at (a) 39.3994s and (b) 10 seconds afterwards.

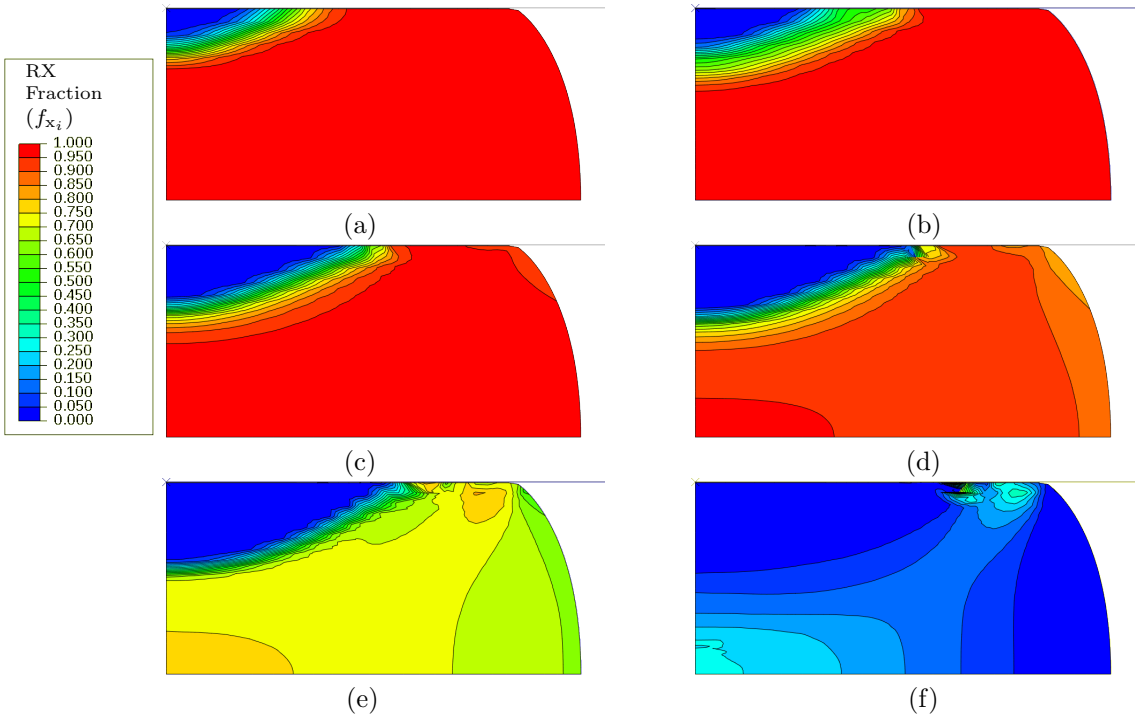


Figure 7: Recrystallized volume fractions (a) $f_{x_1}$, (b) $f_{x_2}$, (c) $f_{x_3}$, (d) $f_{x_4}$, (e) $f_{x_5}$ and (f) $f_{x_6}$ 10 seconds after the simulation.

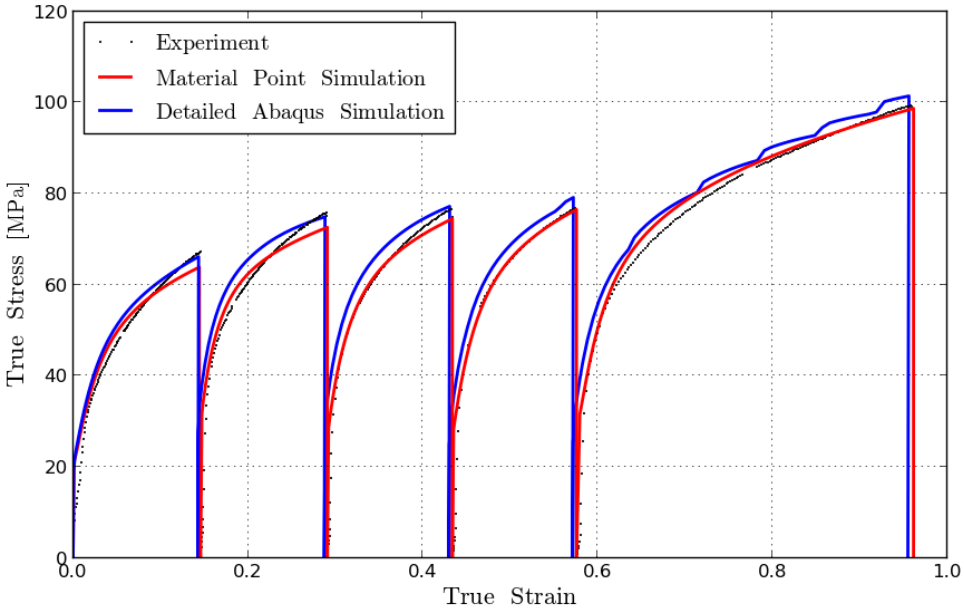


Figure 8: Comparison of the material point integration and the axisymmetric Abaqus simulation true stress vs. true strain results to the experimental data on the schedule $VI$ data with an approximate 10 second wait time between each reduction.

fractions are displayed 10 seconds after the final compression step.

The total reaction force at the mid plane nodes are extracted at each point in the simulation time. The values at these nodes are extracted due to the possibility of roll over at the contact interface. The reaction forces and total displacement from the finite element simulation are used to approximate the true stress over true strain curves. The experimental data, material model response and finite element result are compared in Figure 8.

The finite element results yield slightly larger stress values than those predicted by the material point simulation, but are still reasonably accurate in replicating the experimental results. With confidence in the model's ability to represent the response of the C-Mn-Nb-Ti-V micro-alloyed steel, the through thickness variation of residual stress and internal state variables are presented in the next subsection for a metal slab subject to a three roll pass reduction schedule.

## 5.2 Three roll pass reduction schedule

The material parameter values identified on the C-Mn-Nb-Ti-V alloy in Section 4 can be used to simulate a metal slab subject to a three roll pass reduction schedule. In this schedule, a 300mm thick metal slab is rolled through three sets of double rollers at 1373K(1100°C). The rollers are pressed into the metal slab and a prescribed radial velocity pulls the metal slab through due to contact friction between the rollers and slab.

The tree stage reduction is simulated using a model setup according to the dimensions in Figure 9. Due to symmetry of the problem only half of the slab and three rollers are modeled. Symmetry is enforced using a prescribed boundary condition to restrict movement away from the symmetry plane. Three rollers 950mm in diameter are modeled using analytical rigid surfaces initially spaced with their centers 1000mm away from one another 625mm away from the symmetry plane. The rollers have prescribed displacement and radial velocity boundary conditions. The boundary conditions are applied to the reference point at the center of the roller surface with three degrees of freedom (2 × displacement and 1 × rotation).

A slab section 1000mm long and 150mm high is modeled using 3000 full integration linear plane stain elements. There are 15 elements through the thickness of the half slab modeled. The elements therefore have an initial dimension 5mm long and 10mm high. Hard normal contact is modeled between the upper slab surface and the outer roller surfaces with a friction coefficient $\mu_{\text{frict}} = 0.3$. A prescribed radial velocity is assigned to the reference point's rotational degree of freedom to pull the slab through. This is done using a roll peripheral speed of $1.5\text{ms}^{-1}$ meaning a radial velocity of $\omega = v/r = 1.5\text{ms}^{-1}/0.475\text{m} = 3.15789\text{s}^{-1}$ is used in each case.

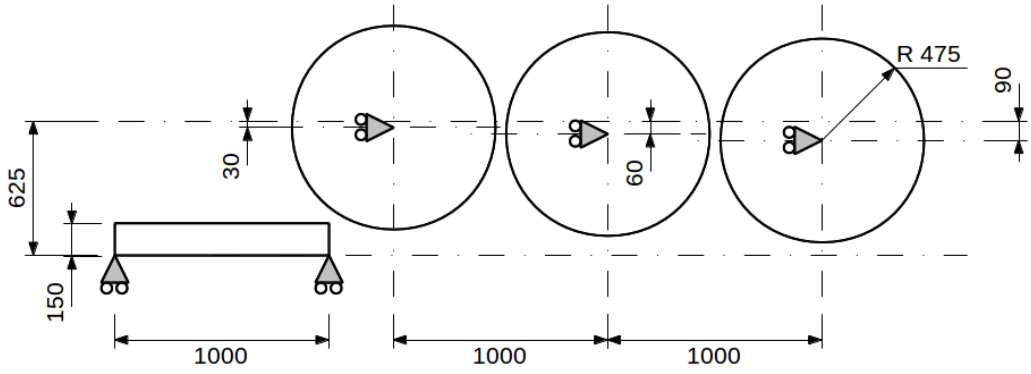


Figure 9: Boundary value problem setup for a three pass roll process.

If each reduction pass reduces the half slab thickness by 30mm, the displaced roller centers are 30mm, 60mm and 90mm away from the original 625mm line respectively as illustrated in Figure 9. This is done in different steps however starting with the right most part of the slab surface just in contact with the first roller. The reduction schedule is modeled in Abaqus using 7 different steps:

- Step 1: A prescribed roller displacement of 30mm is applied over a 1s step time so that the roller is pressed into the slab at the end of the step. A zero roller velocity is applied by fixing the reference point rotational degree of freedom.
- Step 2: A prescribed radial velocity of $3.15789\text{s}^{-1}$ is applied to the first roller. The step time of 0.6667s ensures that at most 1000mm of the slab is pulled through in an ideal case with perfect transfer of the $1.5\text{ms}^{-1}$ roll peripheral speed to the average slab velocity.
- Step 3: During a 10 second interpass time, the first roller is displaced back to the 625mm line while the second roller is displaced to its reduction position 60mm away from the 625mm line. A zero radial velocity is prescribed to all the rollers.
- Step 4: The second reduction roll is modeled with prescribed radial velocity again $3.15789\text{s}^{-1}$ over a 0.6667s step time.
- Step 5: A 10s interpass time where the second roller is displaced back to the 625mm and the third roller displaced 90mm to its final position 60mm away from the symmetry plane. The roller rotational degrees of freedom are again fixed.
- Step 6: The final roll pass at $3.15789\text{s}^{-1}$ over a 0.6667s.
- Step 7: The slab is kept fixed in place for 10 seconds to allow further ISV evolution.

In Figure 10, contours of the von Mises stress, equivalent plastic strain, dislocation density ratio and average slip plane lattice misorientation ISVs are given for the first 30mm reduction roll pass. Contours are also given for the second and third roll pass in Figures 11 and 12. In each case the high stresses $\sigma_{\text{vM}}$ and dislocation density ratios $\bar{\varrho}$ throughout the rolling region decrease further away from the roller to lower residual stress patterns. Apart from the leading end, the equivalent plastic strains and average slip plane lattice misorientation contours show fairly constant through thickness patterns for the first roll in Figure 10(b) and (d) before recrystallization takes place.

The residual stress contours in Figures 11(a) and 12(a) also show a consistent through thickness variation in the rolled slab section. The equivalent plastic strain, dislocation density ratio and misorientation patterns in Figures 11 and 12 show the same kinds of variation or repeatable pattern from one roll to the next.

To better compare and investigate the evolution of the through thickness variation the state quantities can also be extracted along a specific path at different times. The paths of interest in this case are defined from the symmetry plane through the thickness of the slab. Three paths are considered to report through thickness variations for each of the reduction roll passes, each one 500mm down from the three rollers. The field quantities are extracted at each intersection an element edge makes with the path line.

Residual stress values are extracted after each reduction roll pass for example and displayed as a function of the distance from the slab center in Figure 13(a). Residual stresses are reported after the

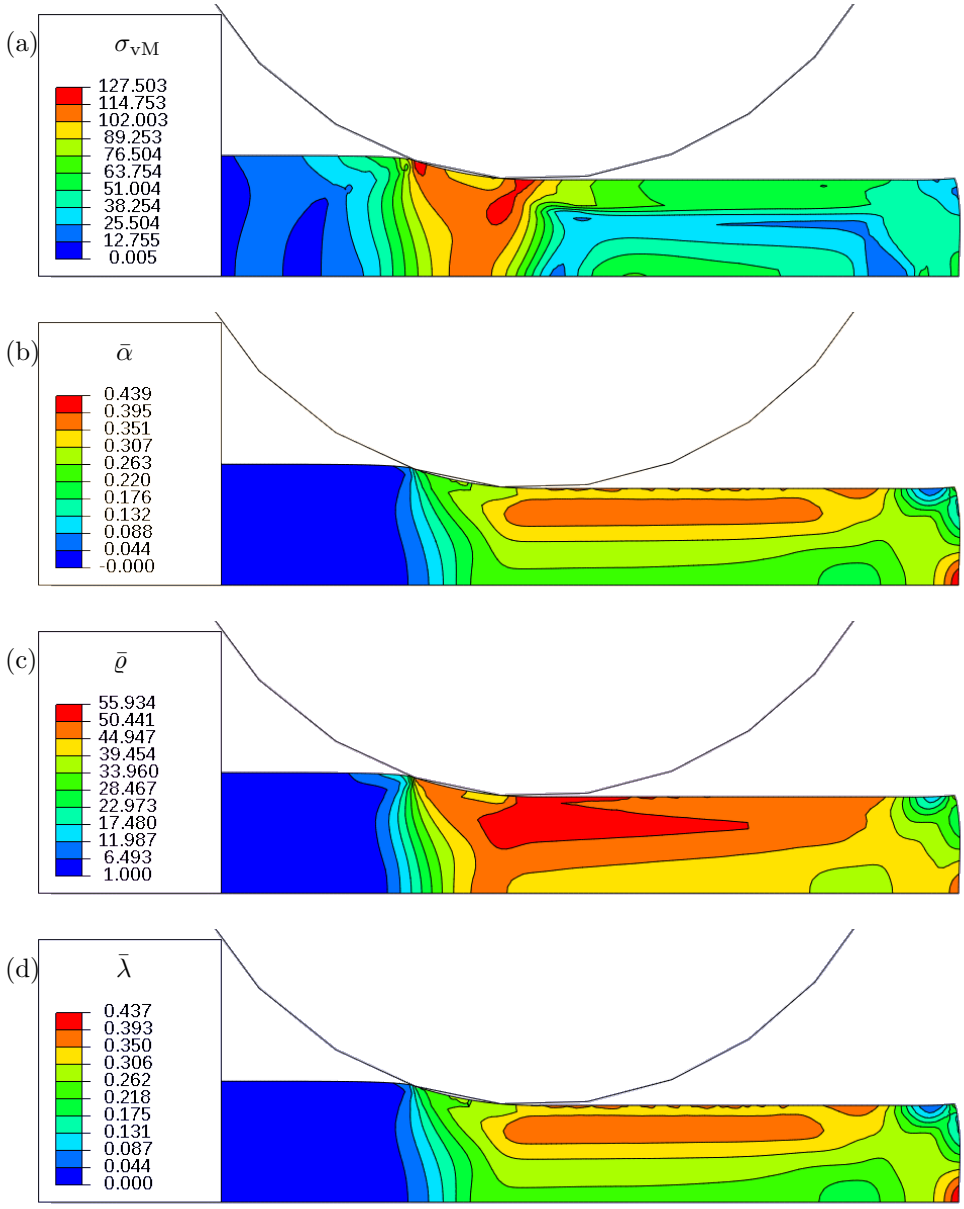


Figure 10: Through thickness contour plots during the first 30mm reduction roll pass. (a) Equivalent von Mises stress. (b) Equivalent plastic strain. (c) Dislocation density ratio. (d) Average slip plane lattice misorientation.

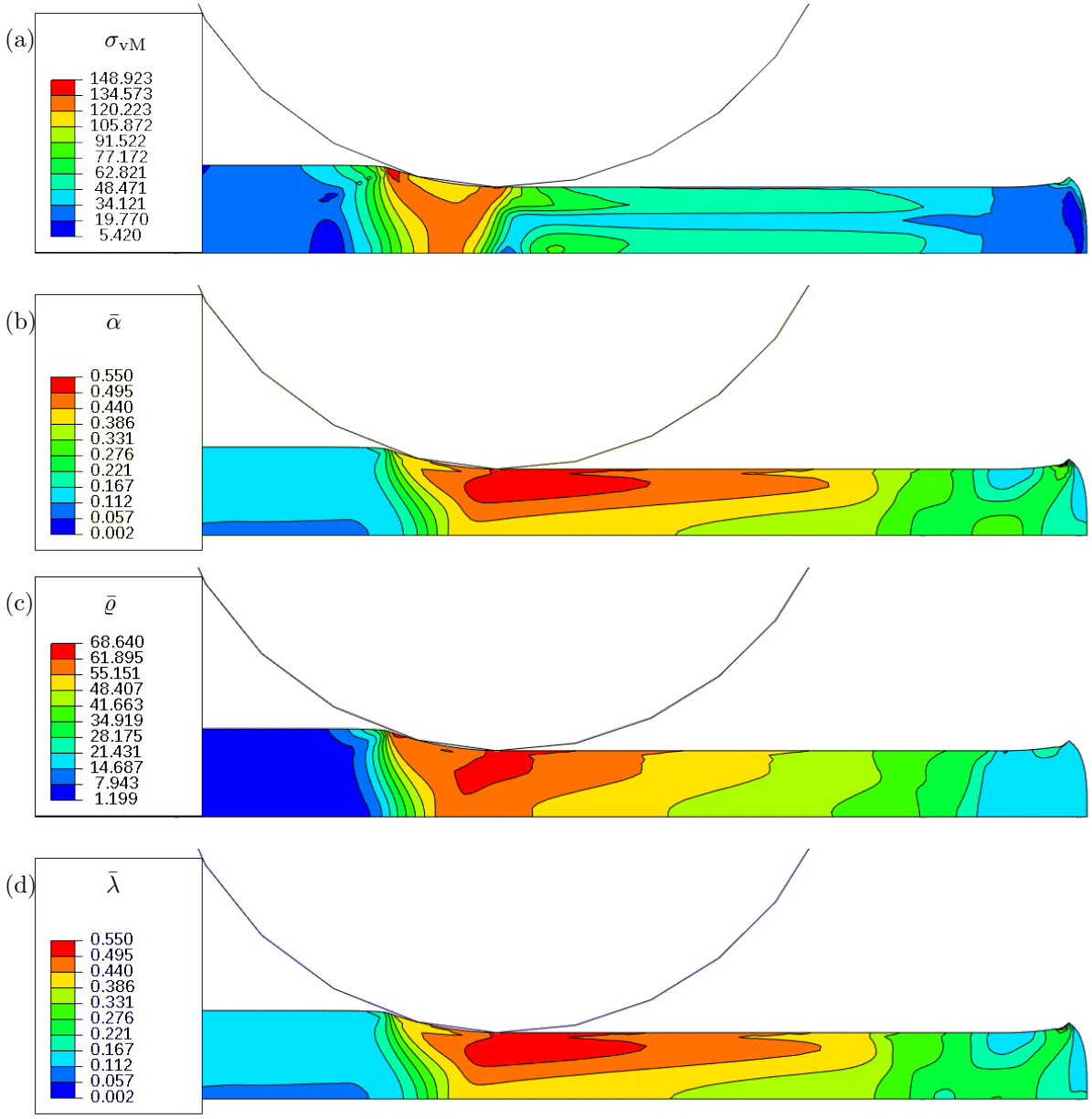


Figure 11: Through thickness contour plots during the second 30mm reduction roll pass. (a) Equivalent von Mises stress. (b) Equivalent plastic strain. (c) Dislocation density ratio. (d) Average slip plane lattice misorientation.

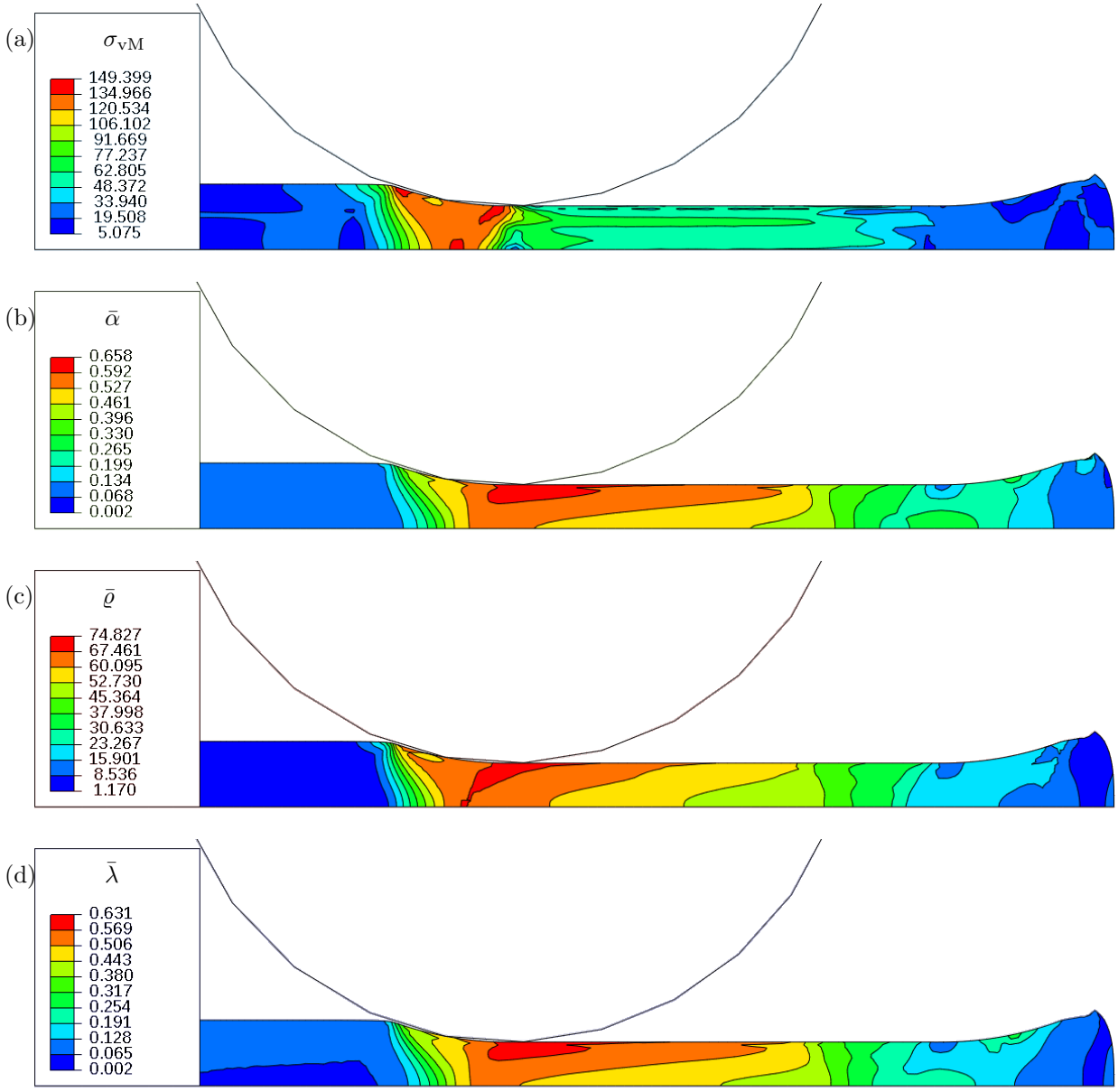


Figure 12: Through thickness contour plots during the final 30mm reduction roll pass. (a) Equivalent von Mises stress. (b) Equivalent plastic strain. (c) Dislocation density ratio. (d) Average slip plane lattice misorientation.

interpass time at the same locations in Figure 13(b). The same is done in Figures 13(c) and (d) for the accumulated equivalent plastic strains. The internal state variables associated with volume fractions recrystallized at least once $f_{x_1}$, twice $f_{x_2}$ and three times $f_{x_3}$ are also extracted and displayed for the different reduction roll passes and interpass times in Figures 13(e) and (f).

The total amount of recrystallization during the first interpass time is visible by considering the blue line plastic strains in Figure 13(c) between 0.2525 and 0.3649 drop to values between 0.1117 and 0.1446 for the blue line in Figure 13(d). This is comparable to between 55.75% and 61.25% recrystallized, also represented by the solid red line in Figure 13(f) since $f_{x_1}$ is the only recrystallized volume fraction ISV active after the first interpass time (I1).

Doing the same comparison on the between 0.345 and 0.4307 equivalent plastic strains in Figure 13(c) and values between 0.0898 and 0.0965 in Figure 13(d) means between 73.97% and 78.04% of the material (original and recrystallized) after the second roll pass is replaced by newly recrystallized material. Some of the material has in fact undergone a second wave of recrystallization considering the I2 $f_{x_1}$ and I2 $f_{x_2}$ lines in Figure 13(f). After the second roll pass between 90.74% and 93.26% of the original material has been replaced by material once recrystallized while between 74.74 and 81.4% of the material volume has undergone two cycles of recrystallization.

After the third roll pass there are three active material volume fractions. Again comparing the through thickness strains in Figure 13(c) with those in Figure 13(d) means that the material is recrystallized between 83.08% and 84.45%. This is evident by red line strain values dropping to between 0.0721 and 0.0813 in Figure 13(d) from values between 0.4264 and 0.5256 in Figure 13(c).

The through thickness variations reported in Figure 13 are as a result of the specific 3×30mm reduction schedule modeled. To further investigate for example the best schedule for a more homogenized through thickness variation, different reduction sequences are modeled and compared as in the following subsection.

## 5.3 Comparing different reduction schedules

The reduction procedure in the previous subsection is repeated with different amounts of reduction per roll pass to investigate an effect on the final through thickness variation. In this subsection six different permutations of a 20mm, 30mm and 40mm reduction are simulated and compared using the problem setup in Figure 9 with different roller displacements. In a permutation where the slab is reduced by 30mm in the first roll, 40mm in the second and 20mm in the final roll pass for example, the displaced roller centers in Figure 9 are now 30mm, 70mm and 90mm instead of the original 30mm, 60mm and 90mm away from the original 625mm line. A roll sequence of 20mm, 30mm, 40mm on the other hand means roller displacements of 20mm, 50mm and 90mm and so on.

The six different possible permutations of 20mm, 30mm and 40mm reduction sequences at 1373K (1100°C) are all again modeled in Abaqus and through thickness variations are extracted along a path 500mm down from the final reduction, 10 seconds after the full sequence. These through thickness variations for the original 3×30mm schedule and the six different permutations of 20mm, 30mm and 40mm reduction sequences are presented for comparison in Figure 14.

According to Figure 14(a) the residual stress patterns through the thickness of the half slab do not vary significantly based on the reduction sequence modeled. There is a variation of around 2-3MPa in the residual stress at a specific distance from the center of the metal slab. The residual plastic strain distribution in Figure 14(b) shows that the 20mm 30mm 40mm reduction sequence end up with the highest average residual plastic strain at around 9.525% while the 40mm 30mm 20mm sequence results the lowest at around 6.272%. The ranking from the most to the least residual plastic strain is shared to a great extent by the volume fraction averaged slip plane lattice misorientation in Figure 14(d).

The 20mm 30mm 40mm sequence also results in the highest volume fraction averaged dislocation density ratio averaged at around 2.9 with 2.56 in the center and 3.57 at the surface of the slab according to the green line in Figure 14(c). The 40mm 30mm 20mm reduction sequence results in by far the most homogenized through thickness dislocation density ratio with an average of 2.21 ranging from 2.203 in the center to 2.19 at the surface while the 3×30mm and 40mm 20mm 30mm sequences have higher values at the surface dropping to around 2.09 at quarter depth where it then remains fairly homogeneous throughout the central part of the slab.

In this study there is a clear effect of the reduction schedule on the through thickness variation of residual stress and internal state variables. The material model may be used within an FEA environment to either assess or improve a roll reduction schedule based on the desired properties of the final product.

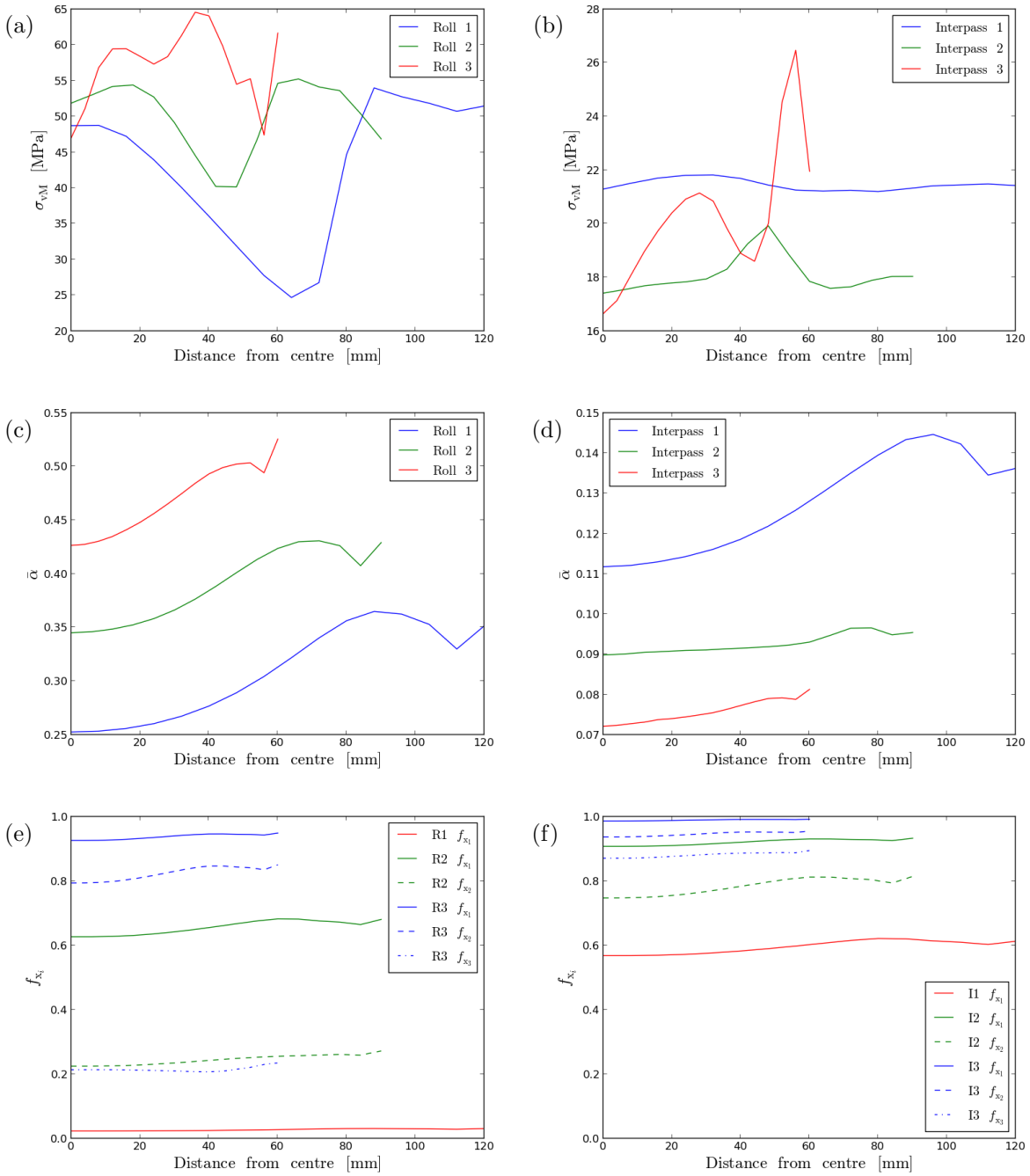


Figure 13: Through thickness material state variations from the center to the surface of the metal slab during the 3×30mm reduction schedule. The von Mises stresses (a) after the roll pass reductions and (b) subsequent interpass times. The equivalent plastic strains (c) after the roll pass reductions and (d) subsequent interpass times as well as volume fractions recrystallized (e) after the roll pass reductions and (f) subsequent interpass times.

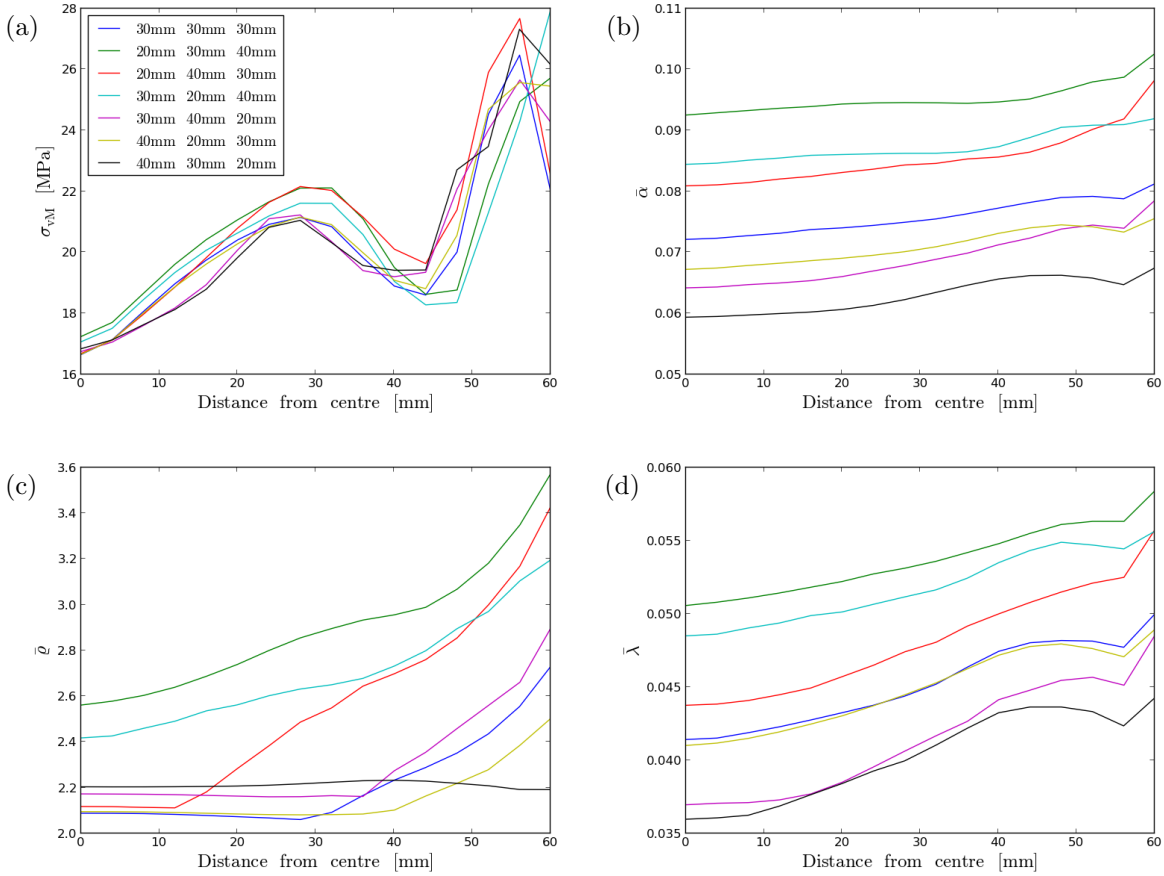


Figure 14: Through thickness variations of the original 3×30mm and six different permutations of 20mm, 30mm and 40mm reduction sequences. (a) $\sigma_{\mathrm{vM}}$, (b) $\bar{\alpha}$, (c) $\bar{\varrho}$ and (d) $\bar{\lambda}$.

# 6 Summary

In this paper a dislocation density based material model was presented to inspect the through thickness variation of material state as a result of different roll reduction schedules on a high strength low alloy steel. The model was characterized to a large set of material response data and also verified against data not used during the characterization. The model has the ability to not only represent the data used in the characterization but also does a fairly good job of predicting material response thanks to the physically motivated deformation mechanisms used in the model development. Use of the model to assess different roll reduction schedules was also demonstrated using a reduction setup of three consecutive roll passes. These different reduction schedules result in different through thickness material state variation. Using the model and methods presented, the desired homogeneity or functional grading of a rolled steel product might now for example be improved by altering a reduction schedule based on finite element simulations.

# References

[1] M. Pietrzyk, C. Roucoules and P.D. Hodgson: *ISIJ Int.*, 1995, vol. 35(5), pp. 531–41.

[2] J. Lin, Y. Liu, D.C.J. Farrugia and M. Zhou: *Phil. Mag.*, 2005, vol. 85(18), pp. 1967–87.

[3] B. Pereda, P. Uranga, D. Stalheim, R. Barbosa and M.A. Rebellato: in *HSLA Steels 2015, Microalloying 2015 & Offshore Engineering Steels 2015: Conference Proceedings*, John Wiley & Sons, Hoboken, NJ, USA, 2015, pp. 309–16.

[4] A. Harun, E. Holm, M. Clode and M. Miodownik: *Acta Mater.*, 2006, vol. 54, pp. 3261–73.

[5] O. Ivasishin, S.S.N. Vasiliev and S. Semiatin: *Mater. Sci. Eng. A*, 2006, vol. 433, pp. 216–32.

[6] F. Chen and Z. Cui: *Model. Simul. Mater. Sc.*, 2012, vol. 20(4).

[7] H. Hallberg and M. Ristinmaa: *Comp. Mater. Sci.*, 2013, vol. 67, pp. 373–83.

[8] E. Popova, Y. Staraselski, A. Brahme, R. Mishra and K. Inal: *Int. J. Plasticity*, 2015, vol. 66, pp. 85–102.

[9] N. Moelans, A. Godfrey, Y. Zhang and D.J. Jensen: *Phys. Rev. B*, 2013, vol. 88, p. 054103.

[10] T. Takaki, C. Yoshimoto, A. Yamanaka and Y. Tomita: *Int. J. Plasticity*, 2014, vol. 52 pp. 105–16.

[11] L. Chen, J. Chen, R. Lebensohn, Y. Ji, T. Heo, S. Bhattacharyya, K. Chang, S. Mathaudhu, Z. Liu and L.Q. Chen: *Comput. Method. Appl. M.*, 2015, vol. 285, pp. 829–48.

[12] P. Zhao, T. Song En Low, Y. Wang and S.R. Niezgoda: *Int. J. Plasticity*, 2016, vol. 80, pp. 38-55.

[13] D. Weygand, Y. Brechet and J. Lepinoux: *Philos. Mag. B*, 1998, vol. 78, pp. 329–52.

[14] Y. Mellbin, H. Hallberg and M. Ristinmaa: *Model. Simul. Mater. Sc.*, 2016, vol. 24(7).

[15] M. Bernacki and R.L.T. Coupez: *Scripta Mater.*, 2011, vol. 64, pp. 525–28.

[16] H. Hallberg: *Model. Simul. Mater. Sc.*, 2013, vol. 21(8).

[17] T.J. Baron, K. Khlopkov, T. Pretorius, D. Balzani, D. Brands and J. Schröder:*Steel Res. Int.*, 2016, vol. 87(1), pp. 37–45.

[18] H. Ji, J. Liu, B. Wang, X. Fu, W. Xiao and Z. Hu: *J. Mater. Process. Tech.*, 2017, vol. 240, pp. 1–11.

[19] F. Montheillet, O. Lurdos and G. Damamme: *Acta Mater.*, 2009, vol. 57(5), pp. 1602–12.

[20] P. Bernard, S. Bag, K. Huang and R.E. Logé: *Mater. Sci. Eng. A*, 2011, vol. 528(24), pp. 7357–67.

[21] H. Riedel and J. Svoboda: *Mater. Sci. Eng. A*, 2016, vol. 665, pp. 175–83.

[22] GJ. Jansen van Rensburg: *Development and Implementation of State Variable Based User Materials in Computational Plasticity.* PhD Thesis, The University of Pretoria, Pretoria, South-Africa, 2016.

[23] A.A. Brown and D.J. Bammann: *Int. J. Plasticity*, 2012, vol. 32–33, pp. 17–35.

[24] R. Maubane, K. Banks, W. Stumpf, C. Siyasiya and A. Tuling: *Adv. Mater. Res.*, 2014, vol. 1019, pp. 339–46.

[25] Y.P. Varshni: *Phys. Rev. B*, 1970, vol. 2(10), pp. 3952–58.

[26] P.S. Follansbee and U.F. Kocks: *Acta Mater.*, 1998, vol. 36(1), pp. 81–93.

[27] Y. Estrin: in *Unified constitutive laws of plastic deformation*, A. Krausz and K. Krausz, eds., Academic Press, San Diego, 1996, ch. 2, pp. 69 – 106.

[28] S. Kok, A.J. Beaudoin and D.A. Tortorelli: *Acta Mater.*, 2002, vol. 50(7), pp. 1653–67.

[29] U.F. Kocks: *J. Eng. Mater-T ASME*, 1976.

[30] J.E. Song and D.L. McDowell: in *Grain Scale Crystal Plasticity Model with Slip and Microtwinning for a Third Generation Ni-Base Disk Alloy.* John Wiley & Sons, Hoboken, 2012, pp. 159–66.

[31] J.W. Cahn and W.C. Hagel: in *Decomposition of Austenite by Diffusional Processes*, Z.D. Zackay and H.I. Aaronson, eds., Interscience, 1962, pp. 131–96.

[32] R.D. Doherty, D.A. Hughes, F.J. Humphreys, J.J. Jonas, D. Juul Jensen, M.E. Kassner, W.E. King, T.R. McNelley, H.J. McQueen and A.D. Rollett: *Mater. Sci. Eng. A*, 1997, vol. 238(2), pp. 219–74.

[33] S.P. Chen, S. Zwaag and I. Todd: *Metall. Mater. Trans. A*, 2002, vol. 33(3), pp. 529–37.

[34] F.J. Humphreys and M. Hatherly: *Recrystallization and Related Annealing Phenomena*, Pergamon, London, 1996.